Electronic Supplementary Material (ESI) for Journal of Materials Chemistry C

Strain evolution in non-stoichiometric heteroepitaxial thin-film perovskites

E. Breckenfeld, A. B. Shah, and L. W. Martin*

Department of Materials Science and Engineering and Materials Research Laboratory, University of Illinois, Urbana-Champaign, Urbana, IL 61801, United States

Supplementary Information

I. Laser Optics and Laser Fluence Determination

For this work, we utilized only imaging mode configurations. More specifically, we focus our laser as an image of an adjustable (circular) iris aperture following the standard procedures in the field (for additional details see, for instance, R. Delmdahl and R. Pätzel, *Phys. Stat. Sol. C* **5**, 3276 (2008)). The laser beam comes out of the laser and passes through a 12.5 mm diameter, circular iris, is then reflected off one 90°, high-quality UV mirrors before passing through a 300 mm focal length lens. The beam then proceeds through a fused silica chamber window and finally strikes the target at a 45° angle. The total optical path is ~150 cm in length and ~15% of the laser energy is lost between the iris and the target (5% at the mirror, 10% at the chamber window). The focusing lens is setup on an adjustable track with the focal point corresponding to the location closest to the window. We always operate with the focusing lens well retracted from the window in an imaging mode.

Laser fluence was determined by measuring the energy of the laser using a calibrated, external energy monitor. Statistics are taken to assure small deviation in the laser energy. Energies are regularly checked prior to and following growths to look for deviations in the laser energy. Optimization of operating voltages was used to assure minimal laser fluence deviation between growths at a given laser fluence. Laser spot sizes were measured using optical microscopy of laser spots on both thermal paper and ceramic TiO_2 targets (chosen for its bright white color and ease of identifying the ablated regime). Following a single laser pulse, on both thermal paper and TiO_2, the surface of the samples is scanned into electrical form using a resolution of 4800 dpi. Images are analyzed using Photoshop and the image analysis software Lispix (www.nist.gov/lispix) to generate a pixel intensity histogram. Using the software, we count the total number of pixels excluding the lightest pixels (which account for less than 2% of all pixels). The dark pixel area is added up to generate the total spot area. A laser spot size of 0.19 cm^2 was used for the growth of all films and fluence was varied by changing the incident laser energy.

II. X-ray Photoelectron Spectroscopy

X-ray photoelectron spectroscopy (XPS) was performed on all samples using a Kratos Axis XPS with a monochromatic Al X-ray source with charge neutralization during collection via electron beam bombardment at an emission angle of 0° from the surface normal. These studies are thought to be sensitive to roughly the top 5-10 nm of the films. The XPS spectra of the Sr 3*d* and Ti 2*p* edges of 10 unit cell thick films of $SrTiO_3$ grown at various laser fluences are provided (Fig.

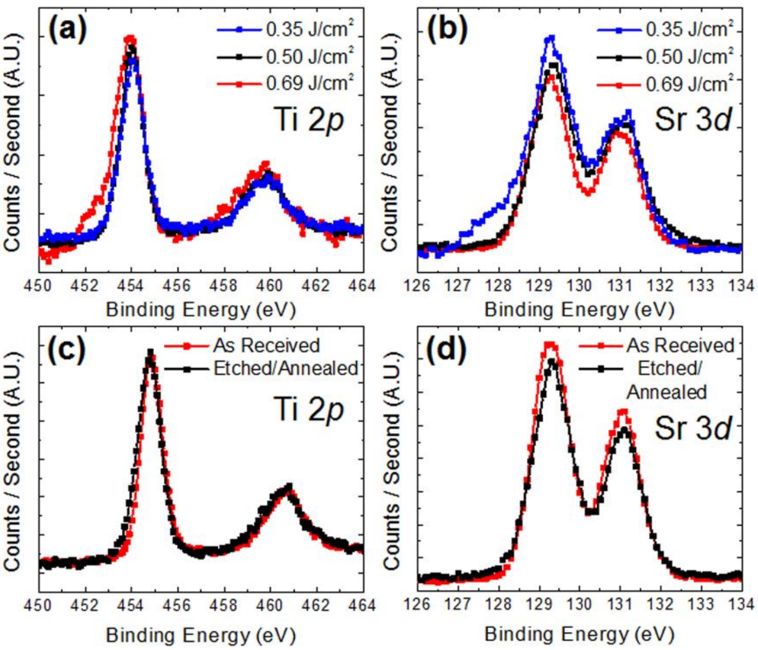

Fig. S1 Typical XPS spectra from films grown at 0.35, 0.50, and 0.69 J/cm^2, (a) Ti 2*p* and (b) Sr 3*d* edges. Typical XPS spectra for as-received and etched and annealed $SrTiO_3$ (001) substrates, (c) Ti 2*p* and (d) Sr 3*d* edges.

S1a and b, respectively). Corresponding XPS spectra of a $SrTiO_3$ substrate used to calibrate the composition of the films are also provided (Fig. S1c and d). Composition was measured and calculated by CasaXPS software. This software quantifies and compares the relative intensities of the relevant core electron peaks (Sr 3*d* and Ti 2*p* in the case of $SrTiO_3$) to obtain the chemical composition with the assumption that the number of electrons recorded is proportional to the number of atoms present within the probed volume. The calibration to the $SrTiO_3$ substrate was done as follows: the composition of the substrate was calculated using a Tougaard background. The relative sensitivity factor of the Sr 3*d* peak was set to the software's published value. The relative sensitivity factor of the Ti 2*p* peak was adjusted until the calculated cation stoichiometry of the substrate matched the manufacturer's compositional report, or 50% Sr. These two relative sensitivity factors were then used for the calculation of the film composition. We do not use XPS to obtain information about the oxygen chemistry of the system, as any *ex-situ* measurements will have minor organic contamination on the surface. These organics will contribute to the oxygen signal, making any information gained from an analysis of the oxygen peaks meaningless with regards to the underlying perovskite.

Note that multiple XPS scans of the $SrTiO_3$ substrate showed a deviation of +/-1% Sr between successive scans for fixed relative sensitivity factors. For this reason, we believe our XPS results to be accurate to within +/-1% Sr. The reported error bars represent this deviation between multiple measurements of the same sample in the XPS system and are meant as a rough estimate of the measurement error from the system. The surface sensitivity of this analysis technique makes the ultimate results sensitive to potential variations or uncertainties in surface termination of the calibration substrate and film. This is clearly demonstrated in Fig. S1c and d, where differences were observed between as-received and etched-and-annealed $SrTiO_3$ substrates.

III. Rutherford Backscattering Spectrometry

We provide a demonstration of the sensitivity of the Rutherford backscattering spectrometry (RBS) studies completed herein. Rutherford backscattering spectrometry (RBS) was performed with an incident ion energy of 2000 keV, incident angle $\alpha = 22.5°$, exit angle $\beta = 52.5°$, and a scattering angle $\theta = 150°$. Fig. S2a shows a wide-range view of data for a nearly stoichiometric $SrTiO_3$ thin film along with the best fit ($Sr_{1.01}Ti_{0.99}O_3$) and fits corresponding to 2%

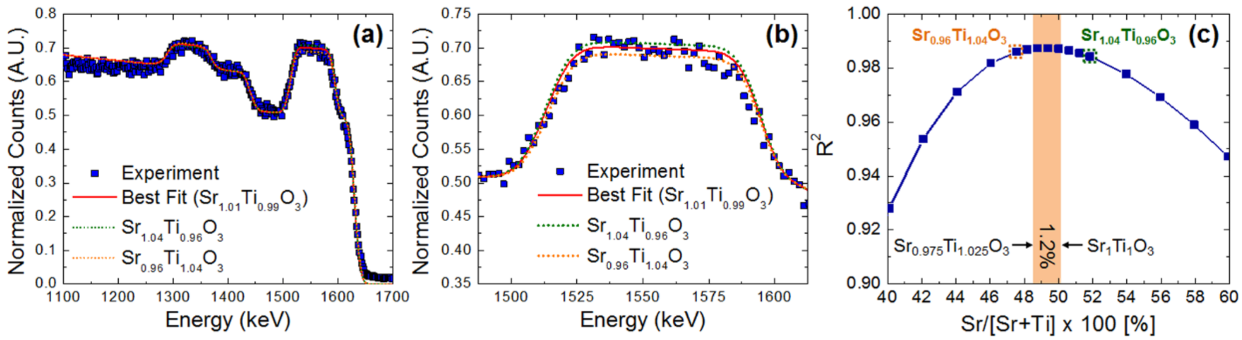

Fig. S2 (a) RBS data for a nearly stoichiometric $SrTiO_3$ thin film along with corresponding fits for stoichiometric, 2% Sr-rich, and 2% Sr-deficient films. (b) Clear distinction between the data and the various models is revealed upon close inspection of the Sr-peak in the RBS data. (c) Determination of the resolution of our RBS measurements. The graph shows the variation in the coefficient of determination (R^2) as a function of various Sr:Ti ratios for models. The resolution is expected to be ~1.2%

Sr-excess ($Sr_{1.04}Ti_{0.96}O_3$) and 2% Sr-deficiency ($Sr_{0.96}Ti_{1.04}O_3$). On this scale, all models fit the data well. Upon closer inspection of, for instance, the Sr-peak in the RBS data (Fig. S2b), a clear discrepancy between the models and data is found. Both the 2% Sr-excess and the 2% Sr-deficiency models bound the data (above and below, respectively). Thus we estimate that for the data reported here we can accurately address the stoichiometry with error bars of approximately 1-2%. This is enough to reveal systematic differences between films grown at various laser fluences and, when combined with the XPS data, reveals systematic trends in the stoichiometry consistent with those reported elsewhere.

The fits reported here were completed using the built-in fitting program in the RBS analysis software SIMNRA (simnra.com). The SIMNRA data fitting program uses a Simplex algorithm for fitting [see J. A. Nelder, R. Mead, Computer Journal **7**, 308 (1965), M. S. Caceci, W. P. Cacheris, Byte **5**, 340 (1984), W. H. Press, B. P. Flannery, S. A. Teukolsky, W. T. Vetterling, *Numerical Recipes*, Cambridge University Press: New York (1988)]. Quantification of the resolution can be achieved by examining the least-squares-fit of a number of models with various Sr/[Sr+Ti]. Here we have investigated the fit of models ranging from 10% Sr-deficiency to 10% Sr-excess (Fig. S2c). The coefficient of determination (so called R^2) or the residual sum of squares divided by the total sum of squares was determined using the following formula:

$$R^2 = 1 - \frac{\sum (y_i - f_i)^2}{\sum (y_i - \bar{y})^2}$$

where the y-values correspond to the intensity of the experimental data and the f-values correspond to the simulated data. The best fits correspond to R^2 values close to 1. We note that for these fits, we focused only on the portion of the experimental data around the Sr- and Ti peaks. The goal of this procedure was to prevent the fits for the substrate peaks form artificially increasing the R^2 values. This, in turn, results in slightly different ideal fits to the data from the holistic, broad spectrum approach used in the SIMNRA-Simplex algorithm, but provides a clear pathway to address the resolution of our data. We have plotted the R^2 value as a function of the Sr/[Sr+Ti] ratio. From the analyses of the data and models, it is found that it is difficult to uniquely differentiate fits of the data between $Sr_{0.975}Ti_{1.025}O_3$ (48.75% Sr) and $Sr_1Ti_1O_3$ (50% Sr). Thus, from the least-squares-fit of the data surrounding only the Sr- and Ti-peaks for the same data as shown in Fig. S2a and b we find the stoichiometry of the film to be $Sr_{0.99}Ti_{1.01}O_3$ which corresponds to 49.4 ± 0.6% Sr. Again, we note that this is slightly different from the fit from the SIMNRA software for this same data (50.5% Sr), but we believe this discrepancy arises from the use of different portions of the data-set. Regardless, this analysis allows us to determine that we can report compositional data to within ~1.2% accuracy

IV. Electron Energy Loss Spectroscopy (EELS)

To local measure the presence of intermixing and to probe defect nature, we employed column-by-column EELS which has a resolution of ~2 Å for both the Ti- and Nd-edges. Using this technique, we can detect differences in electronic structure between adjacent unit cells. Multiple line scans were acquired to confirm the results of the results shown. Microstructural analysis was carried out with a 200 kV JEOL JEM2200FS aberration corrected scanning transmission electron microscope (STEM) coupled with electron energy loss spectroscopy (EELS). Specimens for electron microscopy were mechanically polished and ion milled at 3.5 kV followed by a final polish at 2.0 kV and 0.1 kV. Care was taken to reduce the ion beam current such that the milling rate was less than 2 um/hour. Fig. S3a shows the analysis of EELS from a scan across the thickness of a films posessing Sr-excess chemistry, including a transition across one of the volumetric defects thought to be planar faults of SrO. In these dark regions, the integrated Ti signal drops (as does the integrated oxygen signal) (Fig. S3b). This is indicative of the lack of Ti in there areas and a is consistent with these dark patches being made up of SrO planar faults with coalesce into the triangular patches observed. Additionally, the EEL spectra taken near the film-substrate interface (away from the dark patches) show typical t_{2g}-e_g splitting that is expected for with a Ti^{4+} valence nearly-stoichiometric $SrTiO_3$ while the EEL spectra taken in the dark, triangular patches show reduced t_{2g}-e_g splitting or almost no Ti signal, which indicates the presence of significant Ti^{3+} valence or SrO clustering, respectively.

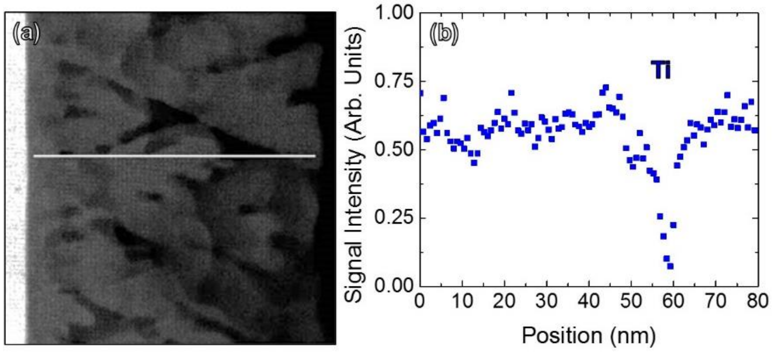

Fig. S3 Electron energy loss spectroscopy for a Sr-deficient film. (a) The location of the linescan across the film is shown. (b) The integrated Ti signal reveals a significant decrease in Ti-content within one of the dark volumetric defect regions.

V. Reciprocal Space Maps (RSMs)

Here we provide a selection of representative RSMs for the various combinations of film compositions and strain states studied herein. RSMs were performed about the 332 and 240 diffraction peaks of $NdGaO_3$ and corresponding 103 and $0\bar{1}3$ diffraction peaks of the $SrTiO_3$. The purple dashed line in the RSMs in Figs. S4 and S5 indicated the Q_y-value of all peaks with the same in-plane lattice parameter as the $NdGaO_3$ substrate. Therefore, all film peaks which fall on this dashed line are coherently strained to the substrate. The black dashed line corresponds to the line along which materials with cubic symmetry would fall, given that combination of in-plane and out-of-plane lattice parameters. Peaks which lie closer to the black line correspond to fully or

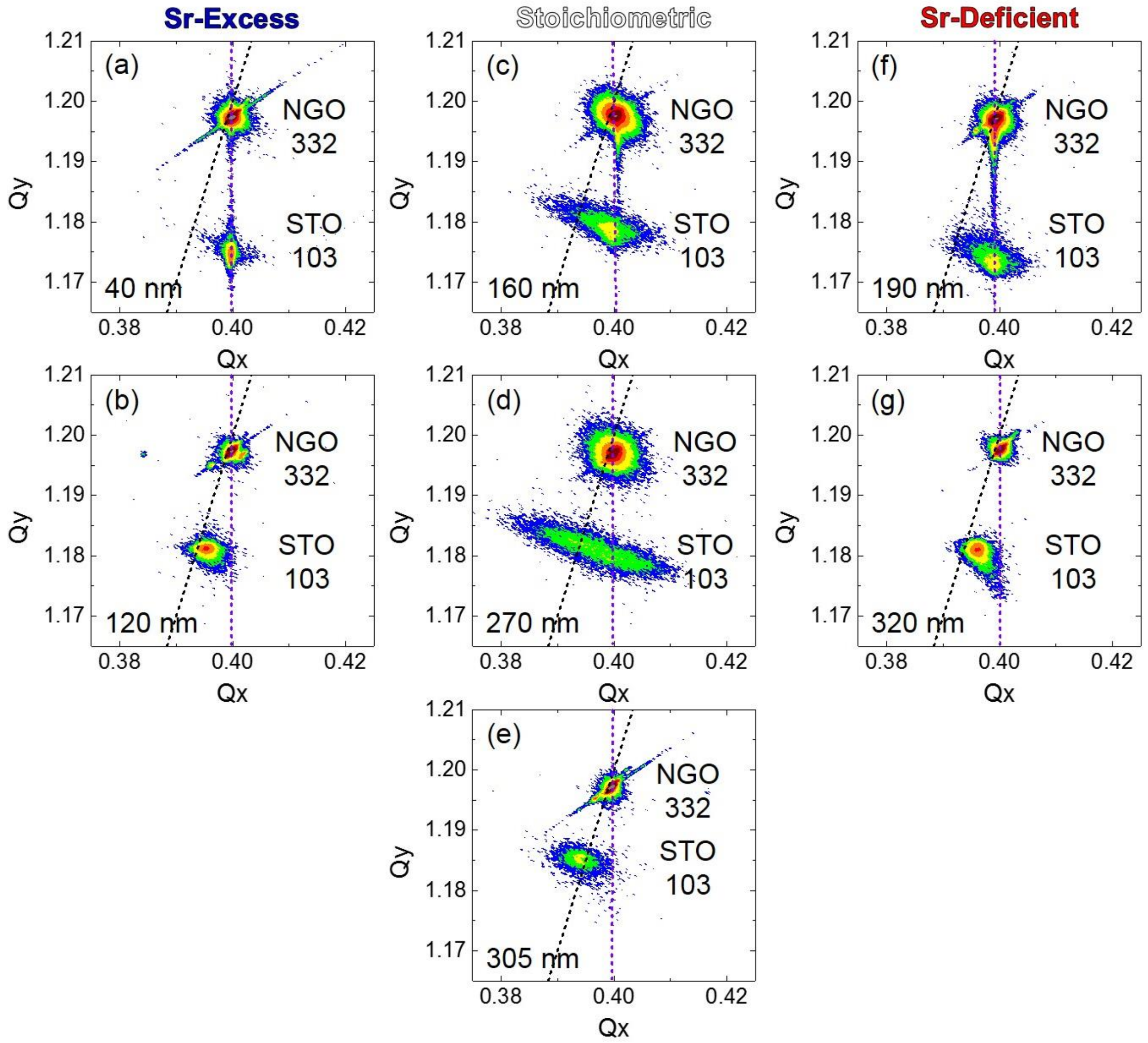

Fig. S4 RSMs of (a) 40nm and (b) 120nm Sr-excess films; (c) 160nm, (d) 270nm, and (e) 305nm stoichiometric films; and (f) 190nm and (g) 320nm Sr-deficient films. All scans are along the substrate 332 diffraction condition.

partially relaxed films. Fig. S4 contains RSMs about the 332 diffraction condition for Sr-excess (Fig. S4a and b), nearly-stoichiometric (Fig. S4c, d, and e), and Sr-deficient (Fig. S4f and g). Figure

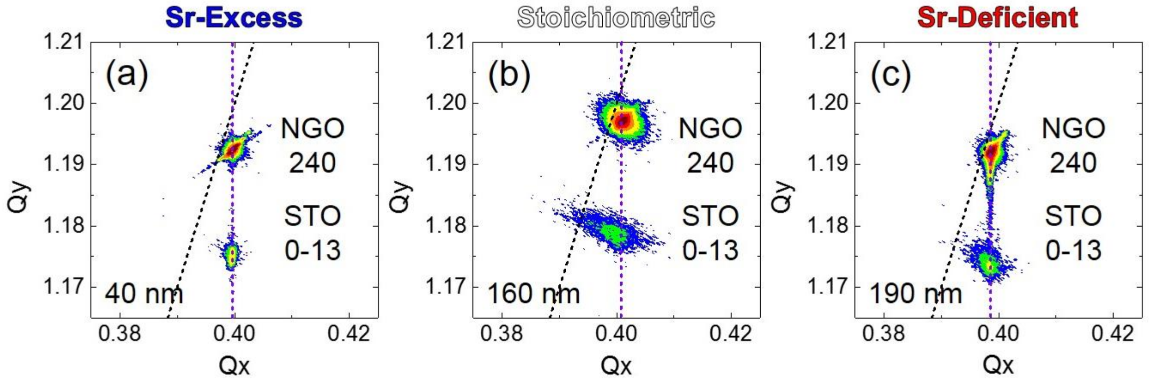

Fig. S5 RSMs of (a) 40nm Sr-excess, (b) 160-nm stoichiometric, and (c) 190nm Sr-deficient films along the substrate 240 diffraction condition.

S4a and b correspond to coherently strained and fully relaxed Sr-excess films, respectively. Figures S4c, d, and e correspond to coherently strained, partially relaxed, and fully relaxed stoichiometric films, respectively. Figures S4f and g correspond to coherently strained and fully relaxed Sr-deficient films, respectively. RSMs about the 240 diffraction condition (Fig. S5) reveal that for all three compositions, when a film is coherently strained, both in-plane lattice parameters are coherently strained to the substrate.